

Article

# Palladium and Graphene Oxide Doped ZnO for Aqueous Acetamiprid Degradation under Visible Light

Carolina Sayury Miyashiro and Safia Hamoudi \* 

Centre in Green Chemistry and Catalysis, Department of Soil Sciences and Agri-Food Engineering, Université Laval, Quebec City, QC G1V 0A6, Canada; carolina-sayury.miyashiro.1@ulaval.ca

\* Correspondence: safia.hamoudi@fsaa.ulaval.ca

**Abstract:** Acetamiprid is a neonicotinoid insecticide widely used in pest control. In recent years, it has been considered as a contaminant in groundwater, lakes, and rivers. Photocatalysis under visible light radiation proved to be an effective process for getting rid of several organic pollutants. In the present work, photodegradation of aqueous acetamiprid was investigated over bare zinc oxide (ZnO) photocatalyst as well as ZnO doped with either palladium or palladium combined with graphene oxide. Both ZnO and doped-ZnO were synthesized via a microwave-assisted hydrothermal procedure. The obtained photocatalysts were characterized using different techniques. After 5 h of reaction at ambient temperature under visible light irradiation, acetamiprid conversions attained ca. 38, 82, and 98% in the presence of bare ZnO, Pd-doped ZnO and Pd-GO-doped ZnO photocatalysts, respectively, thus demonstrating the positive effect of Pd- and GO-doping on the photocatalytic activity of ZnO. In addition, Pd-GO-doped ZnO was shown to keep its activity even when it is recycled five times, thus proving its stability in the reaction medium.

**Keywords:** acetamiprid; degradation; photocatalysis; zinc oxide doping; palladium; graphene oxide



**Citation:** Sayury Miyashiro, C.; Hamoudi, S. Palladium and Graphene Oxide Doped ZnO for Aqueous Acetamiprid Degradation under Visible Light. *Catalysts* **2022**, *12*, 709. <https://doi.org/10.3390/catal12070709>

Academic Editors: Amr Fouda and Mohammed F. Hamza

Received: 20 May 2022

Accepted: 26 June 2022

Published: 28 June 2022

**Publisher's Note:** MDPI stays neutral with regard to jurisdictional claims in published maps and institutional affiliations.



**Copyright:** © 2022 by the authors. Licensee MDPI, Basel, Switzerland. This article is an open access article distributed under the terms and conditions of the Creative Commons Attribution (CC BY) license (<https://creativecommons.org/licenses/by/4.0/>).

## 1. Introduction

The extensive use of insecticides in agriculture fields frequently leads to the contamination of both surface and groundwater streams. Neonicotinoids are currently being recommended as alternatives for organophosphate and carbamate pesticides due to their effectiveness and selective nervous system targeting mechanism [1,2]. Acetamiprid (ACE), a neonicotinoid insecticide, is widely used for the control of sucking-type insects. This insecticide is prone to leaching due to its high solubility in water. Such intrinsic properties may complicate its removal by conventional water treatment technologies [3].

Several processes are currently used for the remediation of contaminated water and wastewaters. Among them, metal oxide semiconductors based photodegradation received growing attention as a favorable application in environmental decontamination. Indeed, heterogeneous photocatalysis is regarded as an advantageous and environmentally friendly technology thanks to its mild operating conditions, high-efficiency, and low-cost [4–7].

Semiconductor metal oxides are characterized by distinctive properties such as chemical stability, tunable compositions, and various morphologies [8]. Among the several current semiconductors, zinc oxide (ZnO) has been extensively utilized in photocatalysis due to its interesting characteristics under UV light. This semiconductor having a direct bandgap energy of 3.37 eV was reported to exhibit a non-toxic nature, a long-lasting photostability, decent optical properties, and high electrochemical stability [9]. Nevertheless, the major disadvantage of ZnO lies in its low photocatalytic activity under visible light, which limits its wide application in advanced oxidation processes implemented for environmental remediation.

To counter this downside, doping was demonstrated to be promising for inducing changes in both physical and chemical properties by incorporating metallic and non-

metallic species leading to a shrink in the ZnO bandgap energy. Therefore, different constituents, encompassing mainly graphene oxide and noble metals, are considered efficient to improve the photocatalytic performances of ZnO in the degradation of organic materials under visible light due to the proven bandgap energy narrowing and the unique electronic orbitals [7,10–12]. Noble metals such as Au [13,14], Ag [15,16], Pt [17], and Pd [18,19] were investigated for doping ZnO photocatalyst. Also, graphene oxide (considered as an electron acceptor) was reported to reduce the recombination of charge carriers [20–22].

Additionally, a variety of conventional methods were applied to produce semiconductors, namely sol-gel [23], mechanochemical [24], and solvothermal [25] methods. Nevertheless, the use of microwave combined with hydrothermal method was emphasized as a judicious synthesis strategy for producing nanostructured materials in a controlled environment. Indeed, microwave energy represents a very efficient means for heating both synthesis as well as reaction media. Photocatalytic materials synthesis, which typically takes a long time to complete, can be undertaken in minutes with the assistance of microwaves. In addition, microwave energy is considered as a reliable, economic, and versatile route of synthesizing various nanostructures [26].

Over the last few decades, removal of several pesticides from water and wastewaters using heterogeneous photocatalysis attracted much attention from the scientific community. However few investigations have been devoted to neonicotinoid insecticides (especially acetamiprid). Also, most of the reported studies carried out the catalytic degradation only under UV light.

In the present investigation, photodegradation of aqueous acetamiprid under visible light was carried out comparatively in the presence of bare ZnO as well as palladium and graphene oxide doped ZnO photocatalysts synthesized via a microwave hydrothermal method.

## 2. Results and Discussion

### 2.1. Photocatalysts Characterization

The morphological and EDX features of ZnO, Pd-ZnO, and Pd-GO-ZnO materials are presented in Figure 1A–D. The bare ZnO material exhibited elongated and irregularly shaped rods and flakes with sharp extremities organized in flower-like structures (See Figure 1A). After doping with palladium, a marked change in the morphology was observed. As illustrated in Figure 1B, better defined and regular rods were observed for the Pd-ZnO material. The sizes of the particles (rods and flakes) were close and ranged between 172 and 190 nm for both materials. As for the Pd-GO-ZnO, it exhibited a completely different morphology revealing monodisperse particles of smaller sizes (ca. 112 nm) in the form of short nanorods decorating the GO sheets (See Figure 1C). This clearly illustrated contact between Pd-ZnO nanoparticles and GO sheets may play an important role in the electronic interactions between both components [27]. The elemental composition spectrum (EDX analyses) confirmed the occurrence of C, Pd, Zn, and O on the Pd-GO-ZnO material (See Figure 1D). The peak of Pd appeared less intense due to its low concentration, the peak of C was attributed to the basal plane of graphene oxide nanosheets, while O was attributed to both ZnO and GO.

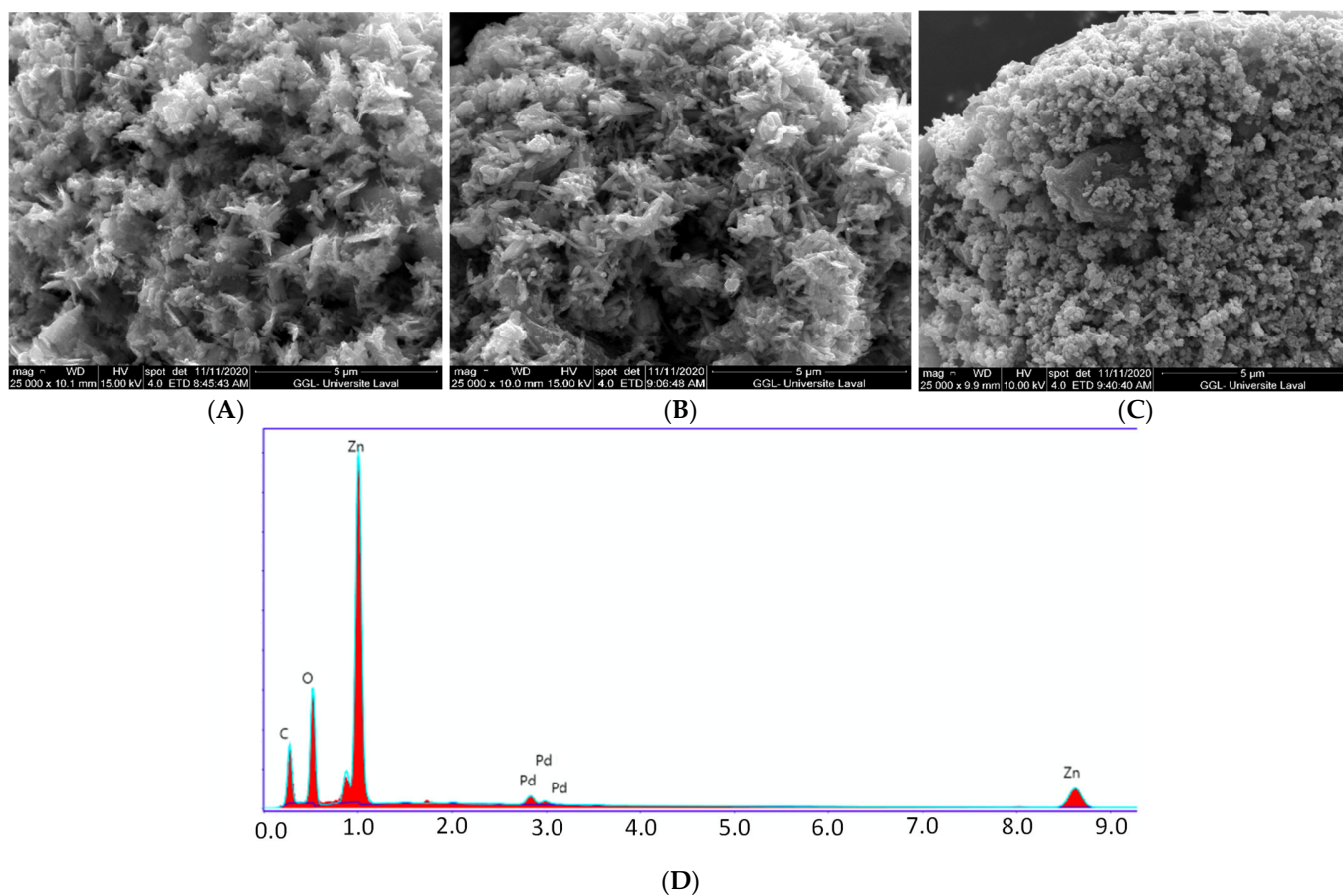


**Figure 1.** SEM images for (A) ZnO; (B) Pd-ZnO; (C) Pd-GO-ZnO; (D) EDX spectrum of the Pd-GO-ZnO-5 material.

The TEM images illustrated in Figure 2A,B indicated the occurrence of very tiny spherical nanoparticles (5–10 nm) aggregated on rods having sizes of about 400 nm length and ca. 50 nm width. In the case of the Pd-ZnO sample (Figure 2B), the tiny particles incorporated in the rodlike structures seemed to be smaller in size compared to the ZnO material. As shown in Figure 2C, the Pd-GO-ZnO material exhibited needlelike structures with 50–200 nm length attached to the GO nanosheets surface.

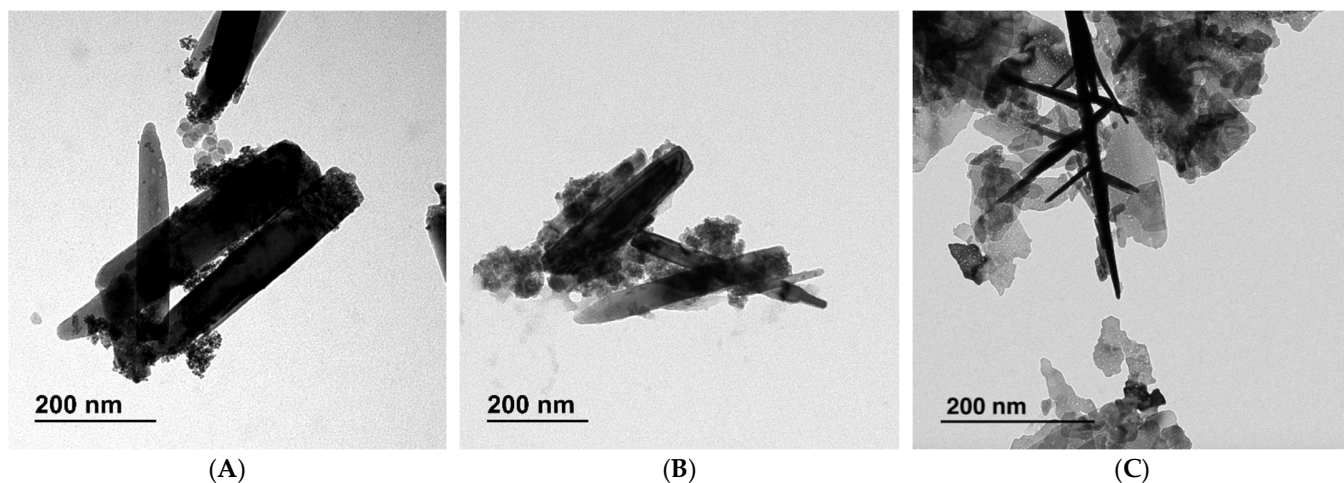


**Figure 2.** TEM images for (A) ZnO, (B) Pd-ZnO, and (C) Pd-GO-ZnO.

The powder diffraction patterns of the ZnO, Pd-ZnO, Pd-GO-ZnO as well as GO materials are presented in Figure 3. The diffractogram belonging to the GO material exhibited a characteristic pattern evidencing a peak at the scattering angle at ca. 11 degrees corresponding to the (001) plane of GO [28]. The diffractograms of the ZnO-containing materials presented strong peaks which can be indexed to the wurtzite-type hexagonal phase of ZnO [29]. The Pd-ZnO material did not exhibit any characteristic peak which could be indexed to Pd or Pd oxide species. This behavior may be attributed to the occurrence of very small crystallite size highly dispersed on the ZnO material [30]. Furthermore, the Pd-GO-ZnO diffractogram did not exhibit neither peaks from GO nor Pd. The absence of Pd peaks may be related to the high dispersion as discussed above. As for the lack of GO characteristic peak, it can be attributed to the reduction of GO into reduced GO during the microwave hydrothermal treatment during the synthesis procedure [31].

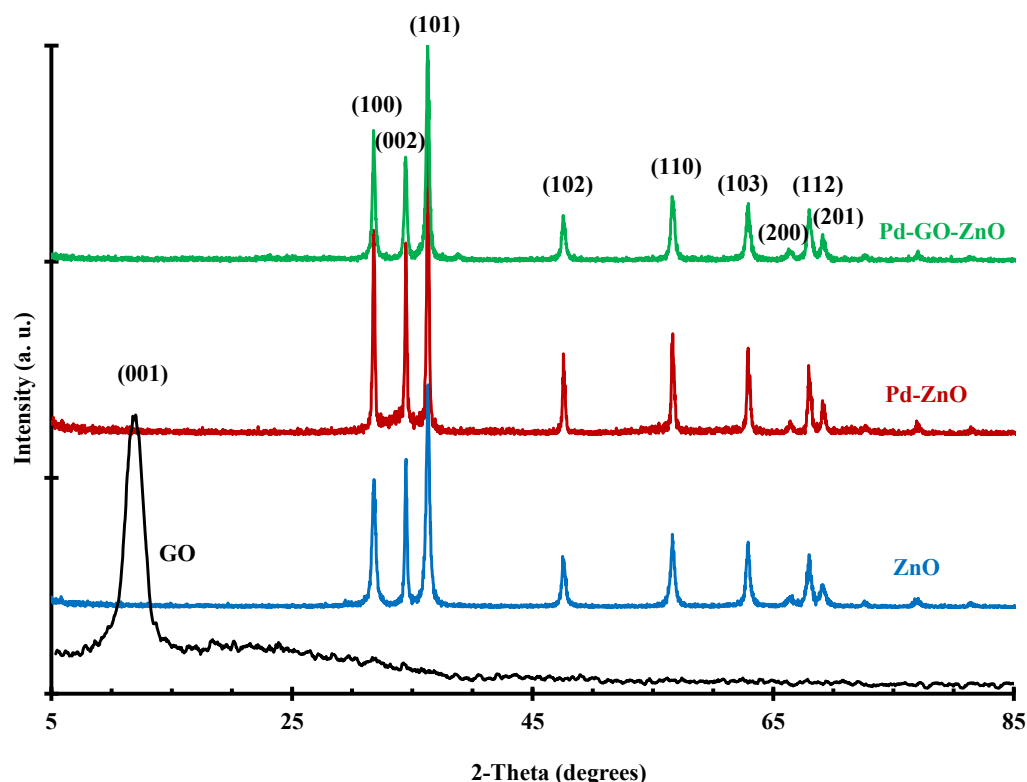


**Figure 3.** Powder XRD patterns of the GO, ZnO, Pd-ZnO and Pd-GO-ZnO materials.

Nitrogen adsorption-desorption volumetric analysis data are illustrated in Figure 4. The isotherms of the photocatalysts were of the type IV, presenting an H3 type hysteresis loop according to the IUPAC classification. These isotherms shapes indicate the occurrence of mesopores (2–50 nm) [32]. Table 1 presents the evaluated textural properties for the different photocatalysts. Interestingly, Pd-ZnO and Pd-GO-ZnO exhibited larger surface areas being 36.27 and 49.52 m<sup>2</sup>/g, respectively, in comparison with the bare ZnO material surface area of 30.90 m<sup>2</sup>/g. Therefore, incorporation of Pd-GO offered an additional advantage with the increase in the surface area, thus providing more active sites and increasing the transport routes for adsorption of acetamiprid molecules which may translate into better photodegradation performances.

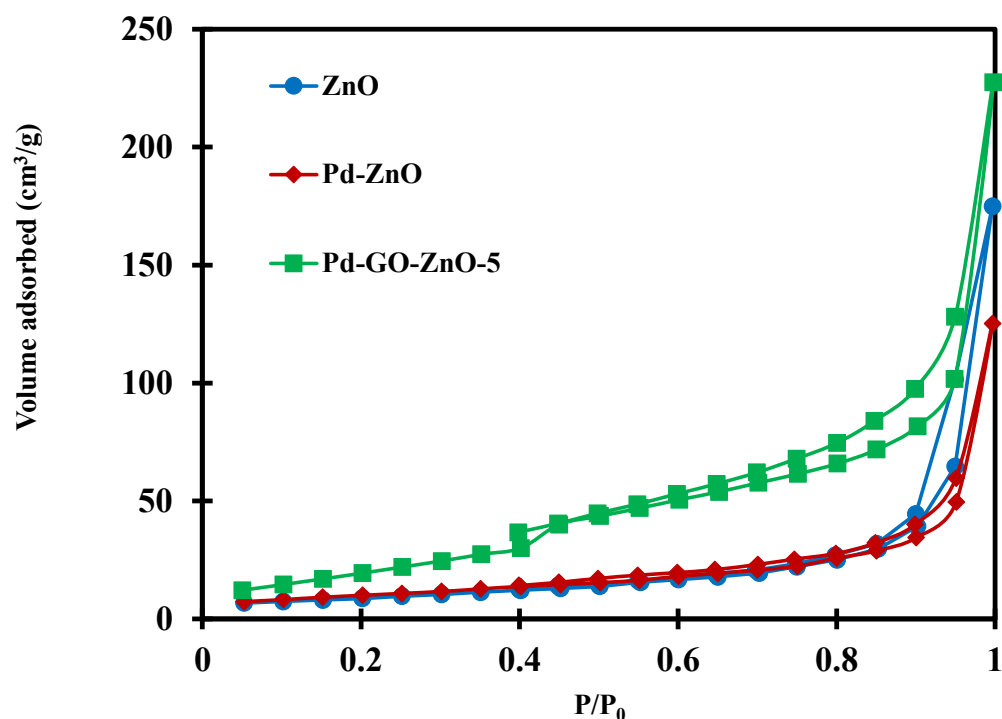


Figure 4. Nitrogen physisorption isotherms of the photocatalysts.

Table 1. Textural properties.

Material	Surface Area (m <sup>2</sup> /g)	Pore Volume (mL/g)	Average Pore Size (nm)
ZnO	30.90	0.27	6.38
Pd-ZnO	36.27	0.19	8.81
Pd-GO-ZnO	49.52	0.18	9.53

The UV-vis absorption spectra of the ZnO, Pd-ZnO, and Pd-GO-ZnO samples measured at room temperature are shown in Figure 5A. The different samples exhibited a large absorption band in the UV region with a shoulder peak located around 375 nm. This shift in the onset of absorption is commonly ascribed to size effects in the photocatalyst, which is characteristic of ZnO broadband semiconductor material [33]. Interestingly, with the incorporation of Pd-GO to the ZnO material, the peak position shifted towards higher wavelengths, indicating a decrease in the optical bandgap of ZnO with GO doping effect. This behavior was attributed to the better separation and transport of the photogenerated charge carriers in the presence of GO [34]. The bandgap energy was determined from Tauc's plots, yielding the optical absorption strength as a function of the photon energy ( $h\nu$ ) using the following Equation:

$$(\alpha h\nu)^2 = A \times (h\nu - E_g) \quad (1)$$

where  $h\nu$  is the photon energy,  $\alpha$  is the absorption coefficient,  $E_g$  is the energy bandgap,  $A$  is constant,  $n$  is 1/2 for allowed direct bandgap. An extrapolation of the linear region of a plot of  $(\alpha h\nu)^2$  versus photon energy ( $h\nu$ ) gives the value of the  $E_g$  as shown in Figure 5B.

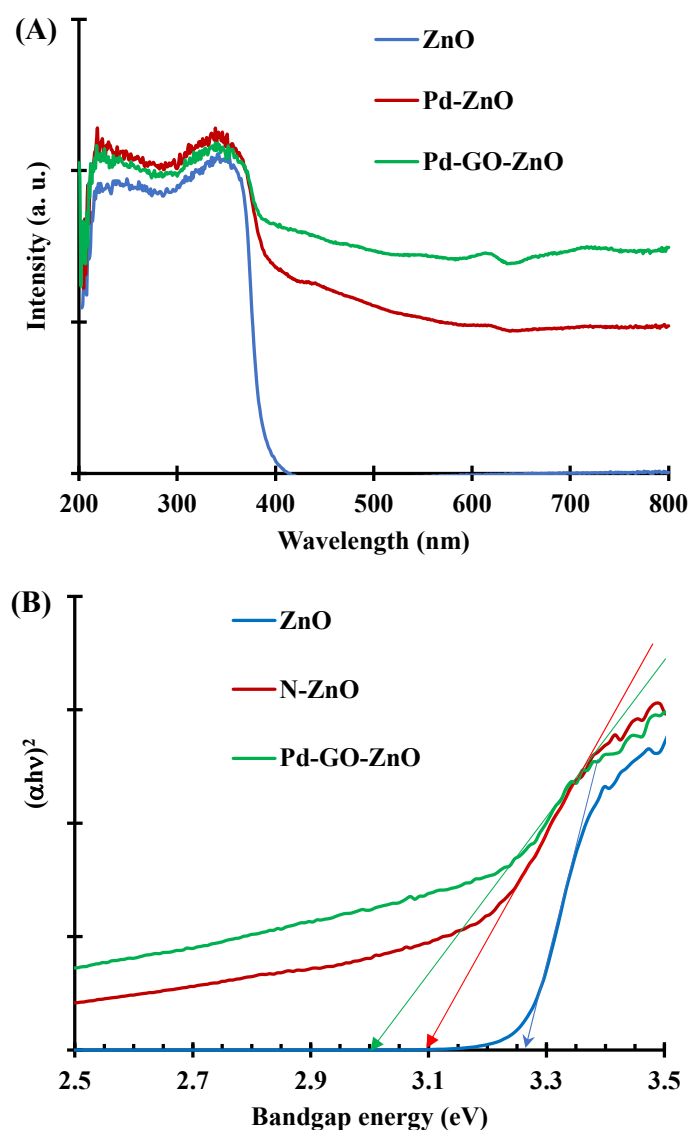


**Figure 5.** (A) UV-vis spectra and (B) estimated bandgap energies from the Tauc plots.

As evidenced in Figure 5B, the bandgap energy was significantly lowered from ca. 3.26 eV for bare ZnO synthesized using microwave to ca. 3.10 and 3.02 eV for the Pd-ZnO and Pd-GO-ZnO, respectively. These results reveal an appreciable reduction in the bandgap energy playing an important role in extending the absorption of doped ZnO to the visible region, which in turn is advantageous to the photocatalytic degradation of organic molecules under visible light [35].

The effect of Pd and GO on the optical properties of the different synthesized photocatalysts was assessed via photoluminescence (PL) spectra measured with a 300 nm excitation at room temperature (Figure 6). The pure ZnO exhibited three PL bands, one in the UV region (band at 400 nm) and two in the visible region (bands at 450 and 500 nm), which can be attributed to either the recombination of free excitons, or impurities, or structural defects encompassing oxygen vacancies, zinc vacancies as well as oxygen and zinc interstitials [36]. The PL intensity of Pd-ZnO and Pd-GO-ZnO-5 was remarkably lowered due to the effective charge transfer from ZnO to Pd-GO in the composites. Moreover, the reduced emission intensity indicates that the electron-hole recombination rate is significantly decreased. This behavior is an asset in the process of photogenerated carriers in the reaction, anticipating better performances in photodegradation reactions [37].

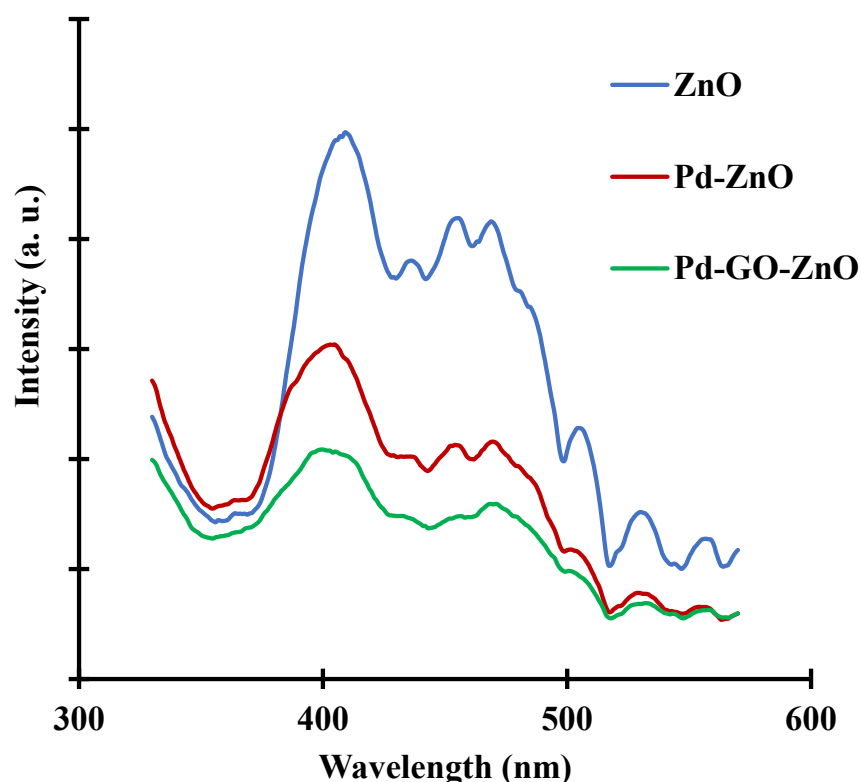


**Figure 6.** Photoluminescence spectra of the photocatalysts.

The XPS survey spectra of the different synthesized photocatalysts demonstrated the occurrence of O, Zn, C and Pd. In the case of bare ZnO and Pd-ZnO, the detected carbon was attributed to the adventitious carbon contamination usually occurring in the analysis of several samples by XPS. Figure 7 shows the high resolution XPS spectra of the ZnO, Pd-ZnO, and Pd-GO-ZnO-5 materials. Since the XPS spectra of the Pd-GO-ZnO samples, containing different amounts of palladium and GO, are quite similar in their characteristics, representative XPS data are reported herein only for the Pd-GO-ZnO-5 together with the data belonging to bare ZnO and Pd-ZnO. The Zn  $2p_{3/2}$  XP core level of the three samples is depicted in Figure 7A. As seen, both samples exhibited symmetric Zn  $2p_{3/2}$  peaks centered at 1022.63, 1022.85 and 1022.95 eV for the bare ZnO, Pd-ZnO and Pd-GO-ZnO-5 samples, respectively. The registered slight shifts towards higher binding energies denote clearly that the chemical environment of the Zn surface atoms was modified upon incorporation of palladium and graphene oxide on the ZnO material. Furthermore, as depicted in Figure 7B for the O1s region, the bare ZnO sample exhibited a peak deconvoluted into two contributing peaks centered at 530.85 and 532.72 eV. These peaks were assigned to the  $O^{2-}$  ions in the wurtzite structure surrounded by the Zn atoms and to the specific chemisorbed oxygen, adsorbed  $O_2$ , or adsorbed  $H_2O$ , respectively [38,39]. Moreover, an additional peak centered at ca. 534.4 eV was observed in the O1s region of the Pd-ZnO and Pd-GO-ZnO samples (Figure 7B), corresponding probably to the formation of metal-oxide such as Pd-O-Zn [40]. As for the Pd $3d_{5/2}$  high resolution spectra presented in Figure 7C, they could be deconvoluted into two contributing peaks centered at 335.35 and 337.49 eV and attributed to metallic palladium Pd(0) and oxidized Pd(II), respectively [41,42].

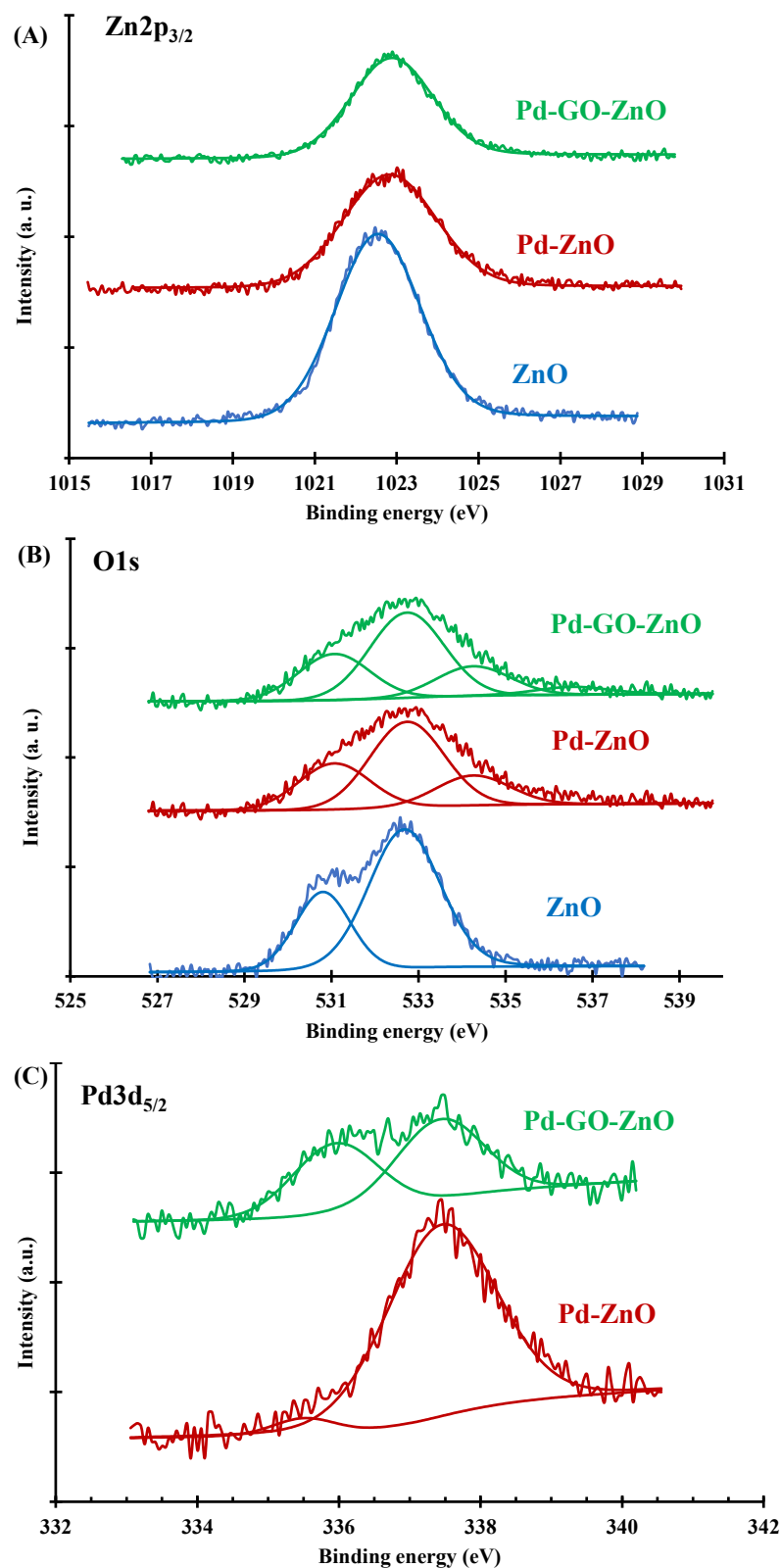
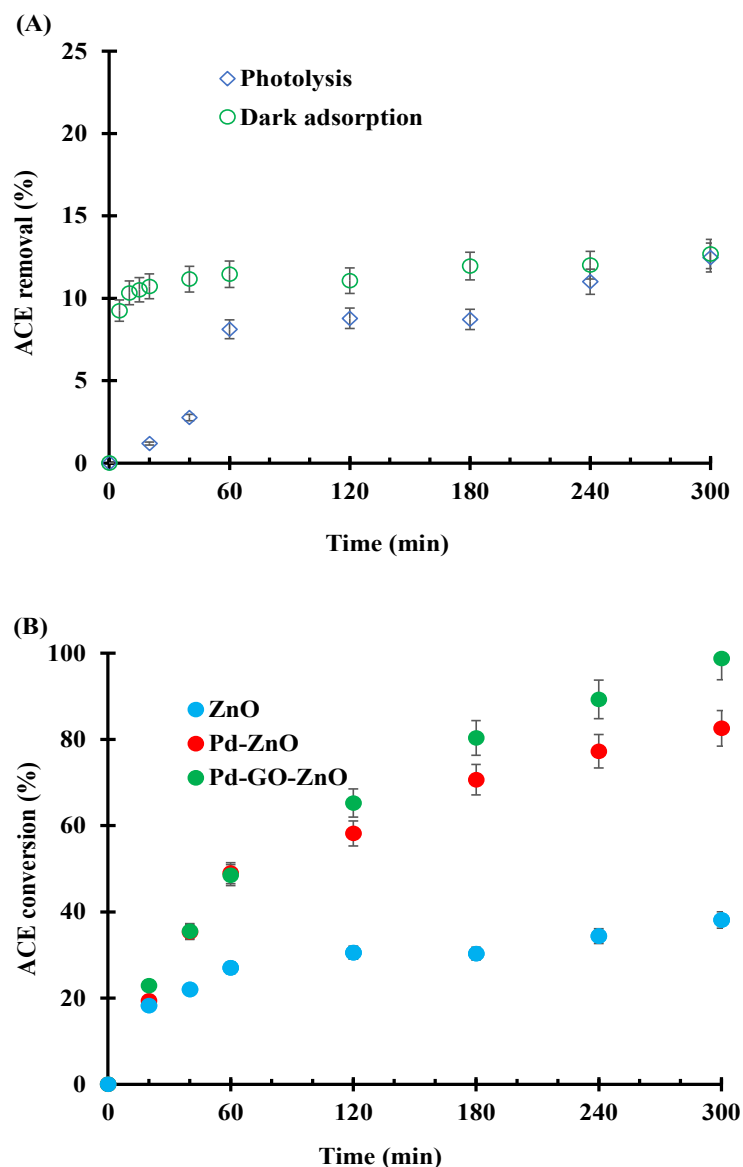


Figure 7. XPS high resolution spectra (A) Zn2p<sub>3/2</sub>; (B) O 1s; (C) Pd3d<sub>5/2</sub>.

## 2.2. Photocatalytic Photodegradation of Aqueous Acetamiprid

Removal tests of aqueous acetamiprid were carried out under dark conditions in the presence of Pd-GO-ZnO as presented in Figure 8A. Acetamiprid adsorption occurred rapidly, and the equilibrium was reached within the first 15 min of contact with the

photocatalytic material as corroborated by the removal time-profile level off at a value of ca. 12% over 5 h of contact. Photodegradation tests of aqueous acetamiprid were performed in the absence of any photocatalyst (photolysis) and over heterogeneous photocatalysts under visible light. The obtained results showed that photolysis allowed to reach only 12% acetamiprid conversion within 5 h of reaction time at ambient temperature (See Figure 8A). Under otherwise the same experimental conditions, the presence of 0.2 g/L of ZnO photocatalyst enhanced the acetamiprid conversion to 38%. With the goal to obtain better performances allowing to get rid of the aqueous acetamiprid, Pd- and Pd-GO-doped ZnO photocatalysts were tested, as reported in Figure 8B.



**Figure 8.** Acetamiprid photolysis and dark adsorption time profiles (A) and acetamiprid photocatalytic degradation time profiles (B). Catalyst loading = 0.2 g/L; Temperature = 25 °C;  $C_0$  = 15 mg/L; Error bars indicate standard deviation.

As evidenced, doping ZnO with palladium resulted in an impressive enhancement of the photocatalytic activity. Indeed, while in the presence of bare ZnO, acetamiprid conversion leveled off at 38% after 5 h of reaction, 82% conversion was reached over Pd-ZnO under the same operating conditions. This fact may be related to the lowered bandgap energy of the doped ZnO and the high activity of the noble metal atoms aggregated on the ZnO surface as evidenced by the EDX and XPS characterizations presented above. Similar behavior

was previously reported for Pd-doped ZnWO<sub>4</sub> composite used for the photodegradation of atrazine [43]. Moreover, the addition of GO to Pd-ZnO caused a significant increase in degradation with 98% acetamiprid conversion obtained over Pd-GO-ZnO-5 after 5 h of reaction. This notable performance may be attributed to the lowered bandgap energy of the composite Pd-GO-ZnO which becomes more active under visible light and to the slowed down recombination of electron-hole pairs, thus improving photocatalytic activity [44]. Also, the formation of hydroxyls and superoxide radicals on the doped photocatalysts surface may be responsible for the enhanced degradation of acetamiprid [28,29,45]. In this connection, a simplified mechanism is suggested for the photocatalytic degradation of the aqueous acetamiprid over the Pd-GO-ZnO photocatalyst (see Figure 9). Also, the detailed reactions leading to the generation of the oxidizing species are summarized in Equations (2)–(9) according to Seddigi et al. [46] and Umukoro et al. [47]:

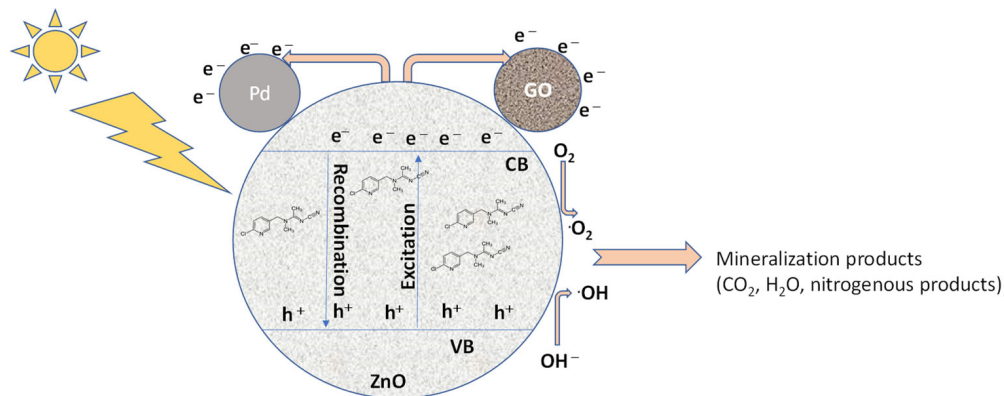
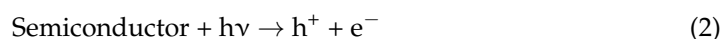


**Figure 9.** The schematic representation of acetamiprid photocatalytic degradation mechanism in the presence of Pd-GO-ZnO under visible light irradiation.

### 2.3. Photocatalyst Stability

Investigation of the photocatalysts stability was conducted using repeated photodegradation tests over the same batch of Pd-GO-ZnO material. Figure 10 presents the obtained acetamiprid conversion data after 4 h of reaction. As can be seen, the photocatalyst activity remained quite stable with conversions fluctuating from ca. 97% to ca. 90% from the first to the fifth cycle. This demonstrates the stability and long lasting nature of the photocatalyst, which makes it worthwhile for use in large-scale applications.

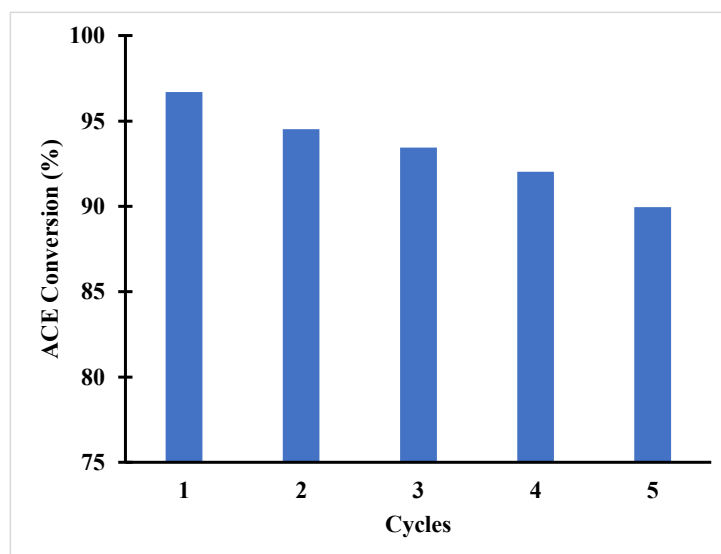


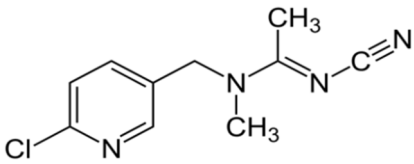
**Figure 10.** Effect of recycling of the Pd-GO-ZnO photocatalyst on acetamidprid conversion. Catalyst loading = 0.2 g/L;  $C_0 = 15$  mg/L; Temperature = 25 °C; Reaction time = 4 h.

### 3. Experimental Methods

#### 3.1. Materials

All reagents were of the highest purity and were used without further purification. Zinc nitrate ( $Zn(NO_3)_2 \cdot 6H_2O$ ) and sodium hydroxide were acquired from JT Baker (Mississauga, ON, Canada). Palladium nitrate hydrate  $Pd(NO_3)_2 \cdot xH_2O$  was purchased from Sigma-Aldrich (St. Louis, MO, USA). For the synthesis of graphene oxide, all of the reagents used were previously reported [48]. Acetamidprid (*N*-(6-Chloro-3-pyridylmethyl)-*N'*-cyano-acetamidine) was purchased from Sigma-Aldrich (Oakville, ON, Canada). The main physicochemical characteristics of this insecticide are summarized in Table 2.

**Table 2.** Acetamidprid physicochemical characteristics.

Chemical Formula	$C_{10}H_{11}ClN_4$
Chemical structure	
Melting point (°C)	98.9
Density (g/mL)	1.33
Solubility in water at 25 °C (mg/L)	$4.25 \times 10^3$
Octanol/water partition coefficient (KOW)	6.27
pKa at 25 °C	0.7
Vapor pressure at 20 °C (mPa)	$1.73 \times 10^{-4}$
Volatility	Low

#### 3.2. Synthesis of ZnO and Pd-ZnO Materials

The ZnO nanocatalyst was synthesized by a microwave-assisted hydrothermal process according to the method reported by Guy et al. [18] with slight modifications. Hence, ZnO was prepared using aqueous solutions of zinc nitrate ( $0.16 \text{ mol L}^{-1}$ ) and sodium hydroxide ( $2 \text{ mol L}^{-1}$ ). A volume of 10 mL of the NaOH solution was added dropwise to a beaker containing 10 mL of the zinc nitrate solution under vigorous magnetic stirring for 1 h to

obtain a uniform mixture. The obtained suspension was placed in a programmable and temperature-controlled microwave furnace (Phoenix from CEM corporation, Mathews, NC, USA) at 160 °C for 5 min. After cooling down to the ambient temperature, the obtained precipitate was removed by centrifugation (5000 rpm), washed several times with distilled water and anhydrous ethanol, then dried in an oven at 100 °C overnight.

The Pd-ZnO material was prepared using the same procedure described above for the ZnO synthesis except that an appropriate amount of palladium nitrate was added to the zinc nitrate solution resulting in a weight ratio Pd/ZnO of 5% before precipitation with an NaOH solution.

### 3.3. Synthesis of the Pd-GO-ZnO Material

The synthesis of graphene oxide (GO) was carried out following the procedure reported by Andrade et al. [48]. After preparation, the Pd-ZnO material was weighed and added to 10 mL of distilled water containing an appropriate amount of GO corresponding to a weight ratio Go/Pd-ZnO of 5%, following a procedure adapted from the work of Yousaf et al. [49]. The obtained material was designated as Pd-GO-ZnO.

### 3.4. Photocatalysts Characterization

The surface morphology of the different synthesized photocatalysts was investigated using a scanning electron microscope (JEOL JSM 840-A, Tokyo, Japan) equipped with an energy-dispersive X-ray spectrometer (EDX) for elemental analysis. The microstructure of the photocatalysts was examined using a transmission electron microscope (JEOL JEM-1230, Tokyo, Japan) at an accelerating voltage of 80 kV. Powder X-ray diffraction (XRD) measurements were carried out on a Rigaku D-Max-Ultima III diffractometer (Rigaku Americas Corporation, The Woodlands, TX, USA) with Cu K $\alpha$  radiation in the 2 $\theta$  range 10–80°. The textural properties of the samples were investigated using nitrogen adsorption/desorption analyses at 77 K using a volumetric adsorption analyzer (Model Autosorb-1, Quantachrome Instruments, Boyton Beach, FL, USA). The optical properties were recorded on a UV-visible spectrophotometer HP UV-8453 (UV-Vis). The photoluminescence (PL) spectra were obtained from a fluorescence spectrometer (Horiba PTI QuantaMaster 8000, Edison, NJ, USA). Survey and high-resolution XPS spectra were recorded using a PHI 5600-ci (Physical Electronics, Chanhassen, MN, USA) spectrometer equipped with an aluminum X-ray source. The main XPS chamber was maintained at a pressure below  $8 \times 10^{-9}$  Torr. The binding energies (B.E.) of core levels in the observed XPS spectra were referenced to C1s core (B.E. at 284.8 eV) [50].

### 3.5. Photocatalytic Tests

Photocatalytic activities were evaluated in a home-made photocatalytic system operating under visible light irradiation at a wavelength  $\lambda > 420$  nm. The visible light source used was 48 W fluorescent bulb irradiating externally the double jacketed reactor and the temperature inside the reactor was controlled by circulating water coming from a temperature-controlled bath through the jacket. The light source was previously preheated before each experiment. Prior to irradiation, the suspensions were stirred for 15 min under dark conditions to ensure the establishment of adsorption/desorption equilibrium between the photocatalyst and acetamiprid solution. The total reactor volume was 300 mL while the reaction volume was 250 mL for a concentration of 15 mg/L acetamiprid, with a catalyst loading of 0.2 g/L under an agitation speed of 600 rpm at room temperature. It is worth noting that the initial concentration of the acetamiprid solution was set to 15 mg/L for the sake of the investigation only. This value is not representative of the environmental concentrations encountered in ground and surface waters which lies between 0.4–5 ng/L but can reach ca. 8  $\mu$ g/L in some agricultural areas where acetamiprid is applied to protect crops [51,52]. The photodegradation reaction time profiles were performed within the time interval of 0–300 min. At preset reaction times, samples of the reactions aqueous suspension were taken, filtered with a micro syringe (0.2  $\mu$ m), solvent extracted and analyzed

for acetamiprid content by gas chromatography. The solvent extraction was carried out according to the method reported by Suganthi et al. [53] with slight modification. Basically a 4 g of acetamiprid reaction sample was accurately weighed in a 15 mL-centrifuge tube and 8 mL acetonitrile were added and vortexed for 20 min. About 1.5 g of anhydrous  $\text{MgSO}_4$  and 0.4 mg NaCl were subsequently added and vortexed. The mixture was then centrifuged for 10 min. After centrifugation, 2 mL of the supernatant aliquot was transferred to a 15 mL centrifuge tube containing 240 mg of anhydrous  $\text{MgSO}_4$ . The mixture was vortexed during a minute and then centrifuged for 10 min. Afterwards, 1 mL of the supernatant was transferred to a vial and concentrated to dryness at 40 °C. The final volume was adjusted to one mL using acetonitrile and transferred to an auto sampler vial for gas chromatography analysis using an HP 6890 Series gas chromatograph equipped with a flame ionization detector (Agilent ChemStation). The column used was an HP-5 measuring 30 m  $\times$  0.25 mm ID  $\times$  0.25 mm film thickness. The injector and detector temperature were adjusted to 250 °C and 1  $\mu\text{L}$  of the sample was injected with a 50:1 split ratio. The oven temperature profile was as follows: initial temperature 100 °C, ramp 10 °C/min at 250 °C, hold for 5 min, ramp 30 °C/min to 300 °C, hold for 5 min. All of the tests reported in the present manuscript were performed in duplicate and analyzed twice.

#### 4. Conclusions

The photocatalytic degradation of aqueous acetamiprid was investigated in the presence of pristine ZnO as well as Pd- and Pd-GO-doped ZnO at room temperature under visible light. Both photocatalysts were successfully synthesized via the microwave assisted hydrothermal technique. The effective doping of Pd and Pd combined to GO was demonstrated through several characterization techniques. Indeed, the bandgap energy of the doped materials was lowered in comparison to bare ZnO. Also, the doped materials exhibited higher surface areas and reduced photoluminescence emission spectra. The best photocatalytic performances were obtained using the Pd-GO-ZnO material which allowed to get rid of the deleterious pesticide water pollutant within 5 h of reaction. Moreover, the doped photocatalyst was shown to be stable even after five reaction cycles, thus confirming its willingness to be used at the industrial scale.

**Author Contributions:** Conceptualization, S.H. and C.S.M.; methodology, C.S.M.; validation, S.H. and C.S.M.; formal analysis, C.S.M.; investigation, C.S.M.; resources, S.H.; data curation, C.S.M.; writing—original draft preparation, C.S.M.; writing—review and editing, S.H.; visualization, S.H. and C.S.M.; supervision, S.H.; project administration, S.H.; funding acquisition, S.H. All authors have read and agreed to the published version of the manuscript.

**Funding:** This research was funded by the Natural Sciences and Engineering Research Council of Canada (NSERC) (Grant No: 2014-05355).

**Data Availability Statement:** All the data generated or analyzed within the present investigation are included in this manuscript.

**Acknowledgments:** Funding provided by the Natural Sciences and Engineering Research Council of Canada (NSERC) and the Canada Foundation for Innovation (CFI) is gratefully acknowledged. The authors would like to thank T. O. Do for the use of the UV-Vis spectrometer.

**Conflicts of Interest:** The authors declare no conflict of interest.

#### References

1. Garrido, I.; Flores, P.; Hellín, P.; Vela, N.; Navarro, S.; Fenoll, J. Solar reclamation of agro-wastewater polluted with eight pesticides by heterogeneous photocatalysis using a modular facility. A case study. *Chemosphere* **2020**, *249*, 126156. [[CrossRef](#)]
2. Morrissey, C.A.; Mineau, P.; Devries, J.H.; Sanchez-Bayo, F.; Liess, M.; Cavallaro, M.C.; Liber, K. Neonicotinoid contamination of global surfacewaters and associated risk to aquatic invertebrates: A review. *Environ. Int.* **2015**, *74*, 291–303. [[CrossRef](#)] [[PubMed](#)]
3. Kanjilal, T.; Bhattacharjee, C.; Datta, S. Biodegradation of acetamiprid from wetland wastewater using indigenous *Micrococcus luteus* strain SC 1204: Optimization, evaluation of kinetic parameter and toxicity. *J. Water Proc. Eng.* **2015**, *6*, 21–31. [[CrossRef](#)]
4. Ahmed, S.N.; Haider, W. Heterogeneous photocatalysis and its potential applications in water and wastewater treatment: A review. *Nanotechnology* **2018**, *29*, 342001. [[CrossRef](#)] [[PubMed](#)]

5. Gusain, R.; Gupta, K.; Joshi, P.; Khatri, O.P. Adsorptive removal and photocatalytic degradation of organic pollutants using metal oxides and their composites: A comprehensive review. *Adv. Colloid Interf. Sci.* **2019**, *272*, 102009. [CrossRef]
6. Vela, N.; Calín, M.; Yáñez-Gascón, M.J.; El Aatik, A.; Garrido, I.; Pérez-Lucas, G.; Navarro, S. Removal of Pesticides with Endocrine Disruptor Activity in Wastewater Effluent by Solar Heterogeneous Photocatalysis Using ZnO/Na<sub>2</sub>S<sub>2</sub>O<sub>8</sub>. *Water Air Soil Poll.* **2019**, *230*, 134. [CrossRef]
7. Miyashiro, C.S. Développement de Catalyseurs Hétérogènes Pour la Photodégradation du Néonicotinoïde Acétamipride Dans L'eau. Ph.D. Thesis, Université Laval, Québec, QC, Canada, 2021. Available online: <https://corpus.ulaval.ca/jspui/handle/20.500.11794/71024> (accessed on 17 June 2022).
8. Júnior, O.G.; Neto, W.B.; Machado, A.E.; Daniel, D.; Trovó, A.G. Optimization of fipronil degradation by heterogeneous photocatalysis: Identification of transformation products and toxicity assessment. *Water Res.* **2017**, *110*, 133–140. [CrossRef]
9. Ong, C.B.; Ng, L.Y.; Mohammad, A.W. A review of ZnO nanoparticles as solar photocatalysts: Synthesis, mechanisms and applications. *Renew. Sustain. Energy Rev.* **2018**, *81*, 536–551. [CrossRef]
10. Ahn, Y.Y.; Yun, E.T.; Seo, J.W.; Lee, C.; Kim, S.H.; Kim, J.H.; Lee, J. Activation of peroxymonosulfate by surface-loaded noble metal nanoparticles for oxidative degradation of organic compounds. *Environ. Sci. Technol.* **2016**, *50*, 10187–10197. [CrossRef]
11. Ghasemi, Z.; Younesi, H.; Zinatizadeh, A.A. Kinetics and thermodynamics of photocatalytic degradation of organic pollutants in petroleum refinery wastewater over nano-TiO<sub>2</sub> supported on Fe-ZSM-5. *J. Taiwan Inst. Chem. Eng.* **2016**, *65*, 357–366. [CrossRef]
12. Hasija, V.; Raizada, P.; Sudhaik, A.; Sharma, K.; Kumar, A.; Singh, P.; Thakur, V.K. Recent advances in noble metal free doped graphitic carbon nitride based nanohybrids for photocatalysis of organic contaminants in water: A review. *Appl. Mater. Today* **2019**, *15*, 494–524. [CrossRef]
13. Vaiano, V.; Jaramillo-Paez, C.A.; Matarangolo, M.; Navío, J.A.; Hidalgo, M.C. UV and visible-light driven photocatalytic removal of caffeine using ZnO modified with different noble metals (Pt, Ag and Au). *Mater. Res. Bull.* **2019**, *112*, 251–260. [CrossRef]
14. Verma, N.; Jagota, V.; Alguno, A.C.; Alimuddin; Rakhra, M.; Kumar, P.; Dugbakie, B.N. Characterization of fabricated gold-doped ZnO nanospheres and their use as a photocatalyst in the degradation of DR-31 dye. *J. Nanomater.* **2022**, *2022*, 7532332. [CrossRef]
15. Wageh, S.; Almazroai, L.; Alshahrie, A.; Al-Ghamdi, A.A. Enhanced visible light photo-catalytic activity of ZnO and Ag-doped ZnO (ZnO:Ag) nanoparticles. *J. Nanosci. Nanotechnol.* **2018**, *18*, 7682–7690. [CrossRef]
16. Kumar, R.; Rana, D.; Umar, A.; Sharma, P.; Chauhan, S.; Chauhan, M.S. Ag-doped ZnO nanoellipsoids: Potential scaffold for photocatalytic and sensing applications. *Talanta* **2015**, *137*, 204–213. [CrossRef]
17. Alahmadi, N.; Amin, M.S.; Mohamed, R. Superficial visible-light-responsive Pt@ZnO nanorods photocatalysts for effective remediation of ciprofloxacin in water. *J. Nanopart. Res.* **2020**, *22*, 230. [CrossRef]
18. Güy, N.; Çakar, S.; Özacar, M. Comparison of palladium/zinc oxide photocatalysts prepared by different palladium doping methods for Congo red degradation. *J. Colloid Interf. Sci.* **2016**, *466*, 128–137. [CrossRef]
19. Najafidoust, A.; Abdollahi, B.; Abbasi Asl, I.; Karimi, R. Synthesis and characterization of novel M@ZnO/UiO-66 (M = Ni, Pt, Pd and mixed Pt&Pd) as an efficient photocatalyst under solar light. *J. Mol. Struct.* **2022**, *1256*, 132580.
20. Li, B.; Liu, T.; Wang, Y.; Wang, Z. ZnO/graphene-oxide nanocomposite with remarkably enhanced visible-light-driven photocatalytic performance. *J. Colloid Interf. Sci.* **2012**, *377*, 114–121. [CrossRef]
21. Yaqoob, A.A.; Noor, N.H.B.M.; Umar, K.; Adnan, R.; Ibrahim, M.N.M.; Rashid, M. Graphene oxide–ZnO nanocomposite: An efficient visible light photocatalyst for degradation of rhodamine B. *Appl. Nanosci.* **2021**, *11*, 1291–1302. [CrossRef]
22. Raliya, R.; Avery, C.; Chakrabarti, S.; Biswas, P. Photocatalytic degradation of methyl orange dye by pristine titanium dioxide, zinc oxide, and graphene oxide nanostructures and their composites under visible light irradiation. *Appl. Nanosci.* **2017**, *7*, 253–259. [CrossRef]
23. Hasnidawani, J.N.; Azlina, H.N.; Norita, H.; Bonnia, N.N.; Ratim, S.; Ali, E.S. Synthesis of ZnO nanostructures using sol-gel method. *Procedia Chem.* **2016**, *19*, 211–216. [CrossRef]
24. Sabri, N.S.; Yahya, A.K.; Talari, M.K. Emission properties of Mn doped ZnO nanoparticles prepared by mechanochemical processing. *J. Lumin.* **2012**, *132*, 1735–1739. [CrossRef]
25. Bai, X.; Li, L.; Liu, H.; Tan, L.; Liu, T.; Meng, X. Solvothermal synthesis of ZnO nanoparticles and anti-infection application in vivo. *ACS Appl. Mater. Int.* **2015**, *7*, 1308–1317. [CrossRef] [PubMed]
26. Sharma, D.; Sharma, S.; Kaith, B.S.; Rajput, J.; Kaur, M. Synthesis of ZnO nanoparticles using surfactant free in-air and microwave method. *Appl. Surf. Sci.* **2011**, *257*, 9661–9672. [CrossRef]
27. Xu, T.; Zhang, L.; Cheng, H.; Zhu, Y. Significantly enhanced photocatalytic performance of ZnO via graphene hybridization and the mechanism study. *Appl. Catal. B* **2011**, *101*, 382–387. [CrossRef]
28. Zhang, Y.; Liu, J.; Zhang, Y.; Liu, J.; Duan, Y. Facile synthesis of hierarchical nanocomposites of aligned polyaniline nanorods on reduced graphene oxide nanosheets for microwave absorbing materials. *RSC Adv.* **2017**, *7*, 54031–54038. [CrossRef]
29. Khurshid, F.; Jeyavelan, M.; Hudson, M.S.L.; Nagarajan, S. Ag-doped ZnO nanorods embedded reduced graphene oxide nanocomposite for photo-electrochemical applications. *R. Soc. Open Sci.* **2019**, *6*, 181764. [CrossRef]
30. Castellazzi, P.; Groppi, G.; Forzatti, P.; Baylet, A.; Marecot, P.; Duprez, D. Role of Pd loading and dispersion on redox behaviour and CH<sub>4</sub> combustion activity of Al<sub>2</sub>O<sub>3</sub> supported catalysts. *Catal. Today* **2010**, *155*, 18–26. [CrossRef]
31. Romeiro, F.C.; Rodrigues, M.A.; Silva, L.A.; Catto, A.C.; da Silva, L.F.; Longo, E.; Lima, R.C. rGO-ZnO nanocomposites for high electrocatalytic effect on water oxidation obtained by microwave-hydrothermal method. *Appl. Surf. Sci.* **2017**, *423*, 743–751. [CrossRef]

32. Hosseini-Sarvari, M.; Razmi, Z.; Doroodmand, M.M. Palladium supported on zinc oxide nanoparticles: Synthesis, characterization, and application as heterogeneous catalyst for Mizoroki–Heck and Sonogashira reactions under ligand-free and air atmosphere conditions. *Appl. Catal. A Gen.* **2014**, *475*, 477–486. [[CrossRef](#)]
33. Hu, Y.; Chen, H.J. Preparation and characterization of nanocrystalline ZnO particles from a hydrothermal process. *J. Nanopart. Res.* **2008**, *10*, 401–407. [[CrossRef](#)]
34. Pudukudy, M.; Yaakob, Z. Facile synthesis of quasi spherical ZnO nanoparticles with excellent photocatalytic activity. *J. Clust. Sci.* **2015**, *26*, 1187–1201. [[CrossRef](#)]
35. Rajeswari, R.; Prabu, H.G. Palladium–Decorated reduced graphene oxide/zinc oxide nanocomposite for enhanced antimicrobial, antioxidant and cytotoxicity activities. *Proc. Biochem.* **2020**, *93*, 36–47. [[CrossRef](#)]
36. Yu, J.; Yu, X. Hydrothermal synthesis and photocatalytic activity of zinc oxide hollow spheres. *Environ. Sci. Technol.* **2008**, *42*, 4902–4907. [[CrossRef](#)]
37. Zhang, J.; Suo, X.; Liu, X.; Liu, B.; Xue, Y.; Mu, L.; Shi, H. PdO loaded WO<sub>3</sub> composite with Na<sub>2</sub>W<sub>4</sub>O<sub>13</sub> flake: A 2-D heterostructure composite material. *Mater. Lett.* **2016**, *184*, 25–28. [[CrossRef](#)]
38. Meng, L.J.; de Sá, C.P.M.; Dos Santos, M.P. Study of the structural properties of ZnO thin films by x-ray photoelectron spectroscopy. *Appl. Surf. Sci.* **1994**, *78*, 57–61. [[CrossRef](#)]
39. Boulares, N.; Guergouri, K.; Zouaghi, R.; Tabet, N.; Lussou, A.; Sibieude, F.; Monty, C. Photoluminescence and photodissociation properties of pure and InO<sub>3</sub> doped ZnO nanophases. *Phys. Status Solidi* **2004**, *201*, 2319–2328. [[CrossRef](#)]
40. Weng, Y.C.; Hsiao, K.T.; Chiu, K.C.; Su, Y.F. The identification and characterization of Ptx-Zn1-xO photocatalysts for photoelectrochemical water splitting applications. *Int. J. Hydrogen Energy* **2016**, *41*, 22997–23006. [[CrossRef](#)]
41. Kemache, N.; Hamoudi, S.; Arul, J.; Belkacemi, K. Activity and selectivity of nanostructured sulfur-doped Pd/SBA-15 catalyst for vegetable oil hardening. *Ind. Eng. Chem. Res.* **2010**, *49*, 971–979. [[CrossRef](#)]
42. Prakhar, S.; Jitendra, K. Fabrication of Graphene-Supported Palladium Nanoparticles-Decorated Zinc Oxide Nanorods for Potential Application. *J. Superconduct. Nov. Magn.* **2019**, *32*, 721–728.
43. Al-Amshany, Z.M.; Hussein, M.A. Novel Pd/ZnWO<sub>4</sub> nanocomposite materials for photocatalytic degradation of atrazine. *Appl. Nanosci.* **2018**, *8*, 527–536. [[CrossRef](#)]
44. Ali, A.; Biswas, M.R.U.D.; Oh, W.C. Novel and simple process for the photocatalytic reduction of CO<sub>2</sub> with ternary Bi<sub>2</sub>O<sub>3</sub>–graphene–ZnO nanocomposite. *J. Mater. Sci. Mater. Electron.* **2018**, *29*, 10222–10233. [[CrossRef](#)]
45. Liu, X.; Pan, L.; Lv, T.; Lu, T.; Zhu, G.; Sun, Z.; Sun, C. Microwave-assisted synthesis of ZnO–graphene composite for photocatalytic reduction of Cr (VI). *Catal. Sci. Technol.* **2011**, *1*, 1189–1193. [[CrossRef](#)]
46. Seddigi, Z.S.; Ahmed, S.A.; Bumajdad, A.; Danish, E.Y.; Shawky, A.M.; Gondal, M.A.; Soylak, M. The efficient photocatalytic degradation of methyl tert-butyl ether under Pd/ZnO and visible light irradiation. *Photochem. Photobiol.* **2015**, *91*, 265–271. [[CrossRef](#)]
47. Umukoro, E.H.; Madyibi, S.S.; Peleyeju, M.G.; Tshwenya, L.; Viljoen, E.H.; Ngila, J.C.; Arotiba, O.A. Photocatalytic application of Pd-ZnO-exfoliated graphite nanocomposite for the enhanced removal of acid orange 7 dye in water. *Solid State Sci.* **2017**, *74*, 118–124. [[CrossRef](#)]
48. Andrade, M.B.; Santos, T.R.; Silva, M.F.; Vieira, M.F.; Bergamasco, R.; Hamoudi, S. Graphene oxide impregnated with iron oxide nanoparticles for the removal of atrazine from the aqueous medium. *Sep. Sci. Technol.* **2019**, *54*, 2653–2670. [[CrossRef](#)]
49. Yousaf, S.; Kousar, T.; Taj, M.B.; Agboola, P.O.; Shakir, I.; Warsi, M.F. Synthesis and characterization of double heterojunction-graphene nano-hybrids for photocatalytic applications. *Ceram. Int.* **2019**, *45*, 17806–17817. [[CrossRef](#)]
50. Gengenbach, T.R.; Major, G.H.; Linford, M.R.; Easton, C.D. Practical guides for x-ray photoelectron spectroscopy (XPS): Interpreting the carbon 1s spectrum. *J. Vac. Sci. Technol. A* **2021**, *39*, 013204. [[CrossRef](#)]
51. Berens, M.J.; Capel, P.D.; Arnold, W.A. Neonicotinoid Insecticides in Surface Water, Groundwater, and Wastewater Across Land-Use Gradients and Potential Effects. *Environ. Toxicol. Chem.* **2021**, *40*, 1017–1033. [[CrossRef](#)] [[PubMed](#)]
52. Zoumenou, B.G.Y.M.; Aina, M.P.; Imorou Toko, I.; Igout, A.; Douny, C.; Brose, F.; Schiffers, B.; Gouda, I.; Sika, K.C.; Kestemont, P.; et al. Occurrence of Acetamiprid Residues in Water Reservoirs in the Cotton Basin of Northern Benin. *Bull. Environ. Contam. Toxicol.* **2019**, *102*, 7–12. [[CrossRef](#)] [[PubMed](#)]
53. Suganthi, A.; Bhuvaneshwari, K.; Ramya, M. Determination of neonicotinoid insecticide residues in sugarcane juice using LC-MS-MS. *Food Chem.* **2018**, *241*, 275–280. [[CrossRef](#)] [[PubMed](#)]